Oxygen Activation by the Noncoupled Binuclear Copper Site in Peptidylglycine α-Hydroxylating Monooxygenase. Spectroscopic Definition of the Resting Sites and the Putative Cu^{II}_M−OOH Intermediate†

Peng Chen,‡ Joseph Bell,§ Betty A. Eipper,§ and Edward I. Solomon*,‡

Department of Chemistry, Stanford University, Stanford, California 94305, and Department of Neuroscience, The University of Connecticut Health Center, Farmington, Connecticut 06030

Received December 18, 2003; Revised Manuscript Received March 11, 2004

ABSTRACT: Spectroscopic methods, density functional calculations, and ligand field analyses are combined to define the geometric models and electronic structure descriptions of the Cu_M and Cu_H sites in the oxidized form of the noncoupled binuclear copper protein peptidylglycine α-hydroxylating monooxygenase (PHM). The Cu_M site has a square pyramidal geometry with a long axial Cu−methionine bond and two histidines, H_2O, and OH^- as equatorial ligands. The Cu_H site has a slightly D_{2d} distorted square planar geometry with three histidines and H_2O ligands. The structurally inequivalent Cu_M and Cu_H sites do not exhibit measurable differences in optical and electron paramagnetic resonance (EPR) spectra, which result from their similar ligand field transition energies and ground-state Cu covalencies. The additional axial methionine ligand interaction and associated square pyramidal distortion of the Cu_M site have the opposite effect of the strong equatorial OH^- donor ligand on the Cu d orbital splitting pattern relative to the Cu_H site leading to similar ligand field transition energies for both sites. The small molecule NO_2^- binds in different coordination modes to the Cu_M and Cu_H site because of differences in their exchangeable coordination positions resulting in these Cu^{II} sites being spectroscopically distinguishable. Azide binding to PHM is used as a spectroscopic and electronic structure analogue to OOH^- binding to provide a starting point for developing a geometric and electronic structural model for the putative Cu^{II}_M−OOH intermediate in the H-atom abstraction reaction of PHM. Possible electronic structure contributions of the Cu^{II}_M−OOH intermediate to reactivity are considered by correlation to the well-studied L3Cu^{II}−OOH model complex (L3 = [HB{3-*t*Bu-5-*i*Prpz}$_3$]). The Met-S ligand of the Cu_M site is found to contribute to the stabilization of the Cu^{II}_M−oxyl species, which would be a product of Cu^{II}_M−OOH H-atom abstraction reaction. This Met-S contribution could have a significant effect on the energetics of a H-atom abstraction reaction by the Cu^{II}_M−OOH intermediate.

Copper proteins play important roles in oxygen binding, activation, and reduction in biological systems (*1*). The copper active sites in these proteins catalyze enzymatic reactions that are often not possible in small molecule chemistry under ambient conditions. A number of these enzymes have binuclear copper active sites, which can be classified as either coupled or noncoupled binuclear sites according to the magnetic interactions between the two copper atoms.

The coupled binuclear copper proteins include hemocyanin, tyrosinase, and catechol oxidase (*2*). The binuclear copper sites in these proteins are strongly antiferromagnetically coupled through a side-on bridging (μ-η^2:η^2) peroxide ligand, which provides a direct mechanism for the initial two-electron reduction of dioxygen to peroxide (*3*). The interaction between the bridging peroxide and the two copper centers leads to their unique spectroscopic features (an intense peroxide π^*_σ to Cu charge transfer (CT) transition at ∼350 nm and the lack of an EPR[1] signal due to antiferromagnetic coupling) and activates the peroxide for electrophilic hydroxylation of enzymatic substrates (*2*, *4*).

The noncoupled binuclear copper proteins include dopamine β-monooxygenase (DβM) and peptidylglycine α-hydroxylating monooxygenase (PHM) (*5*−*8*), which have two Cu sites separated by 11 Å with no bridging ligand and no magnetic interaction. The latter leads to a normal Cu^{II} EPR signal with no spin−spin dipolar coupling. Both enzymes catalyze regiospecific and stereospecific C−H bond hydroxylation reactions of substrates incorporating one oxygen

† This research is supported by NIH Grants DK-31450 (E.I.S.) and DK-32949 (B.A.E.). P.C. has been supported by a Gerhard Casper Stanford Graduate Fellowship and a Franklin Veatch Memorial Fellowship.

* To whom correspondence should be addressed. Phone: 650-723-4694. Fax: 650-725-0259. E-mail: Edward.Solomon@Stanford.edu.

‡ Stanford University.

§ The University of Connecticut Health Center.

[1] Abbreviations: PHM, peptidylglycine α-hydroxylating monooxygenase; PHMcc, catalytic core of PHM; DβM, dopamine β-monooxygenase; CD, circular dichroism; MCD, magnetic circular dichroism; EPR, electron paramagnetic resonance; CT, charge transfer; ET, electron transfer; AcYVG, acetyl-Tyr-Val-Gly; L3, [HB{3-*t*Bu-5-*i*Prpz}$_3$]; LF, ligand field; XAS, X-ray absorption spectroscopy; EXAFS, extended X-ray absorption fine structure; ED, electric dipole; DFT, density functional theory; LUMO, lowest unoccupied molecular orbital.

10.1021/bi0362830 CCC: $27.50
Published on Web 04/17/2004

atom from dioxygen and using ascorbate as the additional physiological reductant (eq 1).

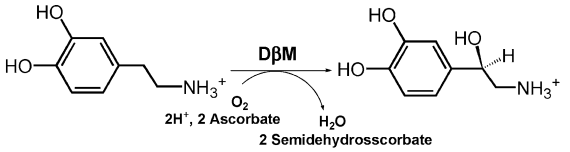

(1a)

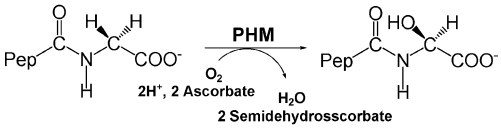

(1b)

The catalytic functions and mechanisms of DβM and PHM are very similar. The catalytic hydroxylation reaction occurs at one Cu site through a H-atom abstraction radical mechanism (*9*−*12*), and the other Cu site supplies an additional electron by long range (∼11 Å) electron transfer (ET). Since the two Cu centers are not coupled, the mechanism of transporting the electron from one site to the other is unclear. A substrate-facilitated ET pathway (either through the substrate (*13*) or through protein residues brought closer upon substrate binding (*14*)) and a superoxide channeling mechanism (*15*) have been proposed for the intercopper ET. At the catalytic site, an as-yet unobserved $Cu^{II}-OOH$ species has been widely proposed as the reactive intermediate for substrate hydroxylation (*5*). A peroxide species, $Cu^{II}-O_2^{2-}$ (or the alternative isoelectronic superoxide form $Cu^{I}-O_2^{-}$), was also proposed as a possibility (*6*). In the past, we have studied a mononuclear hydroperoxide model complex, $L3Cu^{II}-OOH$ (L3 = [HB{3-*t*Bu-5-*i*Prpz}$_3$], hydrotris(3-*tert*-butyl-5-isopropylpyrazolyl)borate), to gain insight into the possible reactivity of the proposed protein $Cu^{II}-OOH$ intermediate (*16*). This $L3Cu^{II}-OOH$ complex is not reactive for H-atom abstraction; spectroscopic and density functional calculations estimate this reaction to be endothermic by ∼45 kcal/mol due to the high energy $Cu^{II}-$oxyl/$Cu^{III}-$oxo product that would be generated after the homolytic O−O bond cleavage.

The crystal structure on the catalytic core of PHM (PHMcc) shows two inequivalent Cu sites in the protein separated by ∼11 Å with no bridging ligation (*13, 17*). The Cu_M site has a distorted tetrahedral geometry with one methionine, two histidines, and a water-derived ligand. The Cu_H site has a nearly square planar geometry with three histidines and one water ligand. The substrate binds at a location close to the Cu_M site with the backbone hydrogen, which is abstracted in the enzymatic reaction, oriented toward at the Cu_M site, identifying the Cu_M as the catalytic site. The Cu_H is then associated with the ET site. Although their structures are clearly different, past spectroscopic studies (e.g., EPR) on oxidized PHM (and DβM) did not find any difference between the two Cu sites (*18, 19*). Controversy also exists concerning the structure of the oxidized Cu_M site where the spectroscopic results suggest a five-coordinate square pyramidal geometry in contrast to the four-coordinate tetrahedral geometry from crystallography (*20*). These would have very different ligand fields. However, Cu d−d transitions have not been observed for this enzyme.

In this study, we combine spectroscopic techniques and density functional calculations to define the geometric and electronic structures of the Cu_M and Cu_H site in resting oxidized PHM. In particular, low-temperature MCD allows the ligand field transitions to be observed for both Cu sites. Their geometric differences are correlated to their spectroscopic similarities through ligand field analyses to understand their indistinguishable spectra. A small molecule binding perturbation approach is found to differentiate the two Cu^{II} site contributions to the EPR and ligand field spectra allowing a correlation to their geometric differences. Parallel spectroscopic studies of structurally defined small model complexes are also presented to facilitate understanding the protein data. The highest occupied π^{nb} molecular orbitals of azide are analogous to the highest occupied π^* orbitals of peroxide/hydroperoxide, both of which have pπ orbitals oriented orthogonal to the molecule axis (*21, 22*). Azide binding is thus used as an electronic and spectroscopic analogue of hydroperoxide to perturb resting PHM and provide a geometric and electronic basis for the putative Cu^{II}_M-OOH intermediate. The electronic structure description developed for the Cu^{II}_M-OOH intermediate is correlated to the $L3Cu^{II}-OOH$ model complex to obtain initial insight into its possible reactivity for H-atom abstraction and serves as a starting point for evaluation of the reaction energetics and mechanism of the enzymatic substrate hydroxylation. Importantly, these studies elucidate the nature of the activation of O_2 for hydroxylation by a single Cu center.

1. EXPERIMENTAL METHODS

Materials. All reagents were of the highest grade commercially available and were used without further purification. The catalytic core of PHM (PHMcc) was expressed and purified as reported (*14*). Enzymatic activities were characterized using acetyl-Tyr-Val-Gly (AcYVG) as the substrate (*14, 23*). AcYVG was obtained from Stanford Protein and Nucleic Acid Biotechnology Facility. All spectroscopic measurements were done at pH ≈ 6.0 in deuterated MES/NaOH buffers. Protein samples were reconstituted with Cu^{II} by incubating with a slight excess of $Cu(NO_3)_2$ in 5−10 μM solution in the same deuterated MES buffer and then concentrated down to the desired protein concentration (∼0.1 mM) in a Millipore Ultrafree centrifugal filter. AcYVG, NaN_3, and $NaNO_2$ solutions were prepared in the same buffer and added into the protein solution for initial incubation and concentration for small molecule perturbation studies. All protein manipulations were done at ∼4 °C. Fifty to sixty percent glycerol-d_3 was added as a glassing agent for low-temperature optical spectroscopy. From CD spectra, glycerol was found not to perturb the Cu^{II} sites. Crystals of model complexes tetrakis(1,2-dimethylimidazole)Cu^{II} di(tetrafluoroborate) ($[Cu^{II}(1,2\text{-dmIm})_4](BF_4)_2$) and tetrakisimidazole$Cu^{II}$ sulfate ($[Cu^{II}(Im)_4](SO_4)$) prepared as in ref *24* were kindly provided by Prof. Harvey J. Schugar (Rutgers).

Spectroscopic Studies. EPR spectra were recorded on a Bruker EMX spectrometer in quartz tubes immersed in a liquid nitrogen finger Dewar. EPR parameters were obtained from simulations using XSophe (*25*). Absorption spectroscopy was performed on a double beam spectrophotometer (Cary 500) equipped with a liquid helium cryostat (Janis Research Super Vari-Temp) or on a HP 8452A diode array spectrophotometer. Circular dichroism/magnetic circular dichroism (CD/MCD) data were collected on CD spectropolarimeters (JASCO J810 with a S20/S1 PM tube for the UV/

vis region and J200 with an InSb detector for the near-IR region) with sample compartments modified to accommodate magnetocryostats (Oxford Instruments, SM4000-7/8T). Due to the weak intensity of the PHM protein MCD signals, a magnetic field dependent but temperature independent background signal was often present. High-temperature 7 T spectra were thus subtracted from low-temperature 7 T spectra to remove this background and obtain the temperature-dependent MCD C-term signals. All spectra presented were normalized to the 5 K 7 T intensity using the Brillouin function for an $S = {}^1/_2$ system (*26*). Extinction coefficients were calculated on the basis of the sample Cu concentrations. Mull samples of the model complexes were prepared by dispersing finely ground powder of the complexes in poly(dimethylsiloxane) (Aldrich) and sandwiching it between two quartz disks.

DFT Calculations. Density functional calculations were performed on a PC cluster using Gaussian 98 (*27*). All calculations were performed using the B3LYP functional (*28*) at the spin-unrestricted level. Two types of basis sets were used as implemented in the Gaussian 98 package. Geometry optimizations and frequencies were calculated with the LanL2Dz basis set. Single point energies were obtained with the triple-ζ TZV basis set. Wave functions were visualized in Molden (*29*) and analyzed with AOmix (*30*).

Ligand Field Calculations. Ligand field calculations were performed using a FORTRAN program written by Cecelia Campochiaro and modified by Elizabeth G. Pavel using the approach developed by Companion−Komarynsky (*31*, *32*).

2. RESULTS

2.1. Spectroscopic. Figure 1A presents the ligand field (LF) region CD/MCD spectra of resting PHMcc. Only two electronic transitions are observed up to 30 000 cm^{-1} in each spectrum, at ∼12 200 and ∼16 700 cm^{-1}, and form a dominant pseudo-*A*-term (i.e., temperature-dependent, derivative-shaped) feature in the MCD spectrum. Resting PHMcc is colorless, and no spectral feature is observed in its UV/vis/NIR absorption spectrum (data not shown). The X-band EPR spectrum of the resting PHMcc shows a typical tetragonal type 2 Cu^{II} signal with $g_z > g_{x,y} > 2.0$ indicating an x^2-y^2 ground state (Figure 1B). Only one type of copper hyperfine coupling is resolved in the g_z region, although there are two inequivalent Cu sites (Cu_M and Cu_H) in the protein. The g_z and A_z values determined from simulations are 2.288 and 157 × 10^{-4} cm^{-1}, respectively (Table 1), consistent with those reported in the literature (*33*). In the presence of substrate, AcYVG, both transitions in the MCD spectrum did not shift in energy relative to those in the resting PHMcc (Figure 1A), indicating that the substrate binding does not perturb the geometries of the Cu sites in resting PHMcc. (The substrate concentrations used here are in the millimolar range, which ensures the complete substrate binding because the K_M(AcYVG) for PHMcc is ∼6 μM (*14*). Note that the intensity difference between the MCD spectra with and without substrate is due to baseline subtraction effects from weak MCD signals and some uncertainty in the sample Cu concentration.)

N_3^- binding shifts the two LF transitions of the resting PHMcc Cu sites only slightly to ∼12 400 and ∼16 400 cm^{-1} in the CD/MCD spectra of PHMcc + N_3^- (Figure 1C).

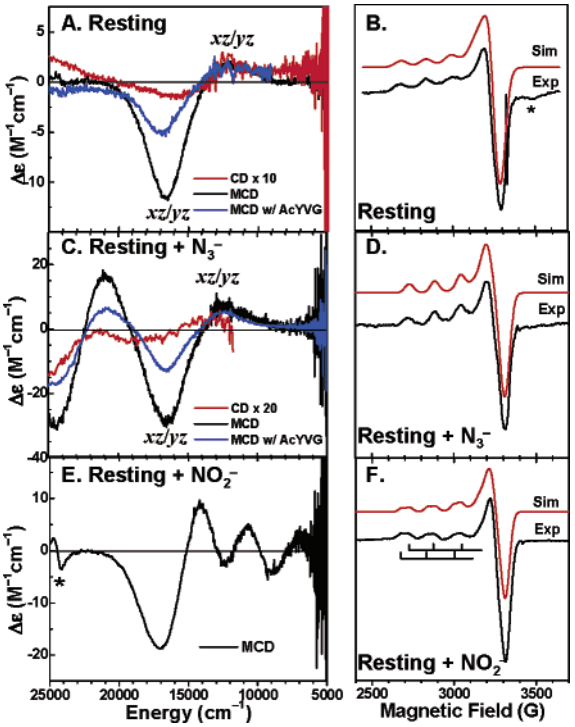

FIGURE 1: (A) Ligand field 5 °C CD and 5 K, 7 T MCD spectra of the resting PHMcc and 5 K, 7 T MCD spectrum of the resting PHMcc with 2−3 equiv of AcYVG substrate; (C) ligand field 5 °C CD and 5 K, 7 T MCD spectra of resting PHMcc with 350 mM N_3^- and the 5 K, 7 T MCD spectrum with an additional ∼4 equiv of AcYVG substrate (The dissociated constant of N_3^- to D*β*M is ∼2 mM (*34*). Considering the similarity between PHM and D*β*M, a similar value for PHM could be reasonably assumed. The concentration of N_3^- used here ensures saturated binding with PHM.); (E) ligand field 5 K, 7 T MCD spectrum of resting PHMcc with 300 mM NO_2^-; (B, D, F) experimental (77 K) and simulated X-band EPR spectra for the resting PHMcc (9.321 GHz), resting PHMcc with 350 mM N_3^- (9.319 GHz), and resting PHMcc with 300 mM NO_2^- (9.394 GHz) samples, respectively. In panel B, "*" denotes a cavity signal. The sharp signal at $g \approx 2.0$ is due to a radical signal of the quartz tube used in the EPR measurement. In panel E, the weak derivative shaped spectral feature at ∼24 500 cm^{-1} ("*") is due to a small heme contaminant.

Table 1: EPR g and A (10^{-4} cm^{-1}) Values[a] and Calculated Ground-State Cu Covalency, β^2 [b]

	g_x	g_y	g_z	A_x	A_y	A_z	β^2
resting	2.050	2.060	2.288	9	12	157	0.70
w/N_3^-	2.040	2.060	2.246	2	25	160	0.66
w/NO_2^-	2.060	2.060	2.265	10	9	160	0.69
	2.060	2.060	2.298	10	9	165	0.73

[a] Complete simulation parameters are given in Table S1. [b] β^2 values were obtained using the equation $A_{\|} = Pd[-\kappa\beta^2 - {}^4/_7\beta^2 + (g_{\|} - 2.0023) + {}^3/_7(g_\perp - 2.0023)]$, where $Pd[Cu^{II}] \approx 400 \times 10^{-4}$ cm^{-1}, $\kappa[Cu^{II}] \approx 0.43$, and $g_\perp = (g_x + g_y)/2$. The signs of experimental $A_{\|}$ (A_z) values are taken as negative (*35*, *36*).

However, new transitions are observed to higher energy in the charge-transfer region. The MCD spectrum shows three new transitions at ∼21 000 (+), ∼24 500 (−), and ∼28 600 (−) cm^{-1} (Figure 2B). Two new transitions are also observed in the CD spectrum in the CT region at ∼25 800 (−) and ∼29 900 (+) cm^{-1} (Figure 2B). In this energy region of the absorption spectrum of PHMcc + N_3^-, moderately intense charge-transfer features are observed at ∼26 000 cm^{-1} with $\epsilon \approx 3400$ $M^{-1}cm^{-1}$ (Figure 2A), giving the solution a pale yellowish color. The energy and intensity of this absorption

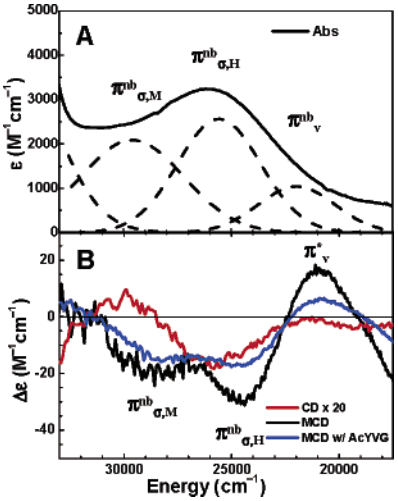

FIGURE 2: (A) Charge-transfer absorption spectrum (5 °C) of resting PHMcc with 350 mM N_3^- (dashed lines are Gaussian fitted bands); (B) Charge-transfer 5 °C CD and 5 K, 7T MCD spectra of resting PHMcc with 350 mM N_3^- and 5 K, 7 T MCD spectrum with ~4 equiv of substrate AcYVG added to PHMcc + N_3^-. Gaussian fitted CD and MCD spectra of resting PHMcc + N_3^- are given in Figure S2.

band are consistent with the results of previously reported N_3^- binding studies on DβM (*34*). Simultaneous Gaussian fit of the absorption, CD, and MCD spectra of PHMcc + N_3^- in the CT region gives three transitions at energies of 21 950, 25 550, and 29 600 cm^{-1} with extinction coefficients of ~1050, 2550, and 2100 M^{-1} cm^{-1}, respectively (Figure 2A). Since binding a single N_3^- to a single Cu^{II} can produce only two CT transitions (from the N_3^- π_σ^{nb} and π_v^{nb} orbitals), the presence of three bands indicates that two N_3^- bind to the Cu^{II} sites.

The X-band EPR spectrum of the N_3^--bound form of PHMcc also shows only one type of tetragonal Cu^{II} signal (Figure 1D). However, a smaller g_z is observed (2.246, Table 1), and the line widths in the g_z region become much narrower relative to those of resting PHMcc. Combined with the fact that three N_3^- CT transitions are observed in absorption/CD/MCD, this indicates that both Cu^{II} centers are perturbed by N_3^- binding with one N_3^- to each Cu^{II}. A similar EPR g value perturbation by N_3^- binding was also observed for DβM (*34*). Similar to resting PHMcc, the addition of substrate AcYVG to PHMcc + N_3^- did not change the MCD spectra (Figure 1C and 2B), indicating that substrate binding does not perturb the Cu sites of N_3^--bound PHMcc. This is consistent with previous infrared studies on CO binding to the reduced PHMcc, which showed that substrate binding does not perturb the vibrational frequency of CO bound at the Cu_M site (*15*).

NO_2^- can bind to biological Cu active sites (e.g., in nitrite reductase) and also form Cu^{II} complexes in either monodentate or bidentate ligating mode (*37*). Previous studies using NO_2^- as a perturbing small molecule provided a wealth of information about geometric and electronic structures of Cu^{II} sites (*38*). NO_2^- is thus used here to provide an additional handle to probe the Cu^{II} sites in PHM. Since the protein sample was concentrated through a membrane filter, any exogenous Cu^{II} was washed out, and the observed spectra are from protein-bound Cu^{II}. Possible binding of NO_2^- to PHM other than the Cu sites cannot be determined here

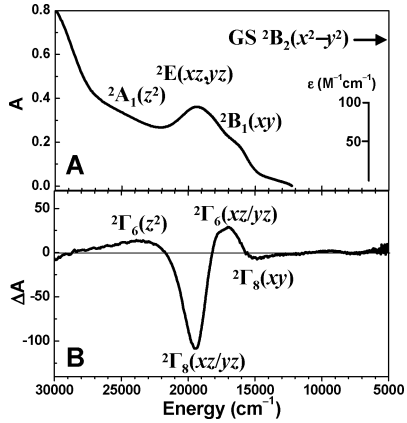

FIGURE 3: Mull absorption (10 K, A) and mull MCD spectra (5 K, 7 T, B) of $[Cu^{II}(1,2\text{-dmIm})_4](BF_4)_2$. The symmetry symbols in panel A give assignments in the D_{2d} group, and those in panel B give assignments in the S_4' double group (reference Scheme 1 and section 3.1.1). The ϵ scale is from literature values measured from solution spectrum (*24*). The structural parameters of $[Cu^{II}(1,2\text{-dmIm})_4](BF_4)_2$ were taken to be similar to those of the $[Cu^{II}(1,2\text{-dmIm})_4](ClO_4)_2$ complex, of which the crystal structure is available and shown in Figure S1 (*39*).

because the spectroscopic techniques used here only detect signals associated with the paramagnetic Cu^{II} centers. The addition of 300 mM (~1500-fold) NO_2^- significantly perturbed the MCD and EPR spectra of resting PHMcc. (The addition of 30 mM (~150-fold) NO_2^- gave partial conversion.) Six transitions are now observed in the MCD spectrum at ~6900 (+), ~8900 (−), ~10 700 (+), ~12 350 (−), ~14 200 (+), and ~17 000 (−) cm^{-1} (Figure 1E), as compared to the two-band spectrum of the resting PHMcc (Figure 1A). Since one Cu^{II} site can at most contribute four d−d transitions, the presence of six LF bands in the MCD spectrum indicates that both Cu_M and Cu_H sites in PHMcc are contributing and spectroscopically differentiated. In parallel, the X-band EPR spectrum of the NO_2^--perturbed PHMcc shows two sets of Cu^{II} hyperfine couplings in the g_z region with approximately equal intensity, consistent with two inequivalent Cu sites (Figure 1F). The g_z values of these two EPR signals, 2.265 and 2.298, are different from the value of the resting PHMcc, further indicating that both Cu sites in the protein are perturbed. This is the first time that the two Cu sites in oxidized DβM or PHM could be spectroscopically differentiated. This is also consistent with the presence of three N_3^- to Cu CT bands in the MCD spectrum of PHMcc + N_3^- indicating two inequivalent Cu^{II} sites (see section 3.3.1).

To facilitate the analysis of the PHMcc protein spectra, parallel spectroscopic studies were performed on two structurally defined tetragonal Cu^{II} imidazole complexes. Figure 3 presents the low-temperature mull absorption and MCD spectra of the $[Cu^{II}(1,2\text{-dmIm})_4](BF_4)_2$ complex, which has an approximately square planar geometry with four equatorial imidazole ligands. One dominant transition is observed in the absorption spectrum at ~19 000 cm^{-1} with a low-energy shoulder around 16 000 cm^{-1} (Figure 3A). The extinction coefficients for these two transitions are about 50−100 M^{-1} cm^{-1} (*24*). Four transitions are observed in the MCD spectrum at ~15 500 (−), ~17 000 (+), ~19 500 (−), and ~23 000 (+) cm^{-1} (Figure 3B). The middle two transitions in the MCD spectrum correspond to the strong absorption band at ~19 000 cm^{-1} (Figure 3A) and form a dominant

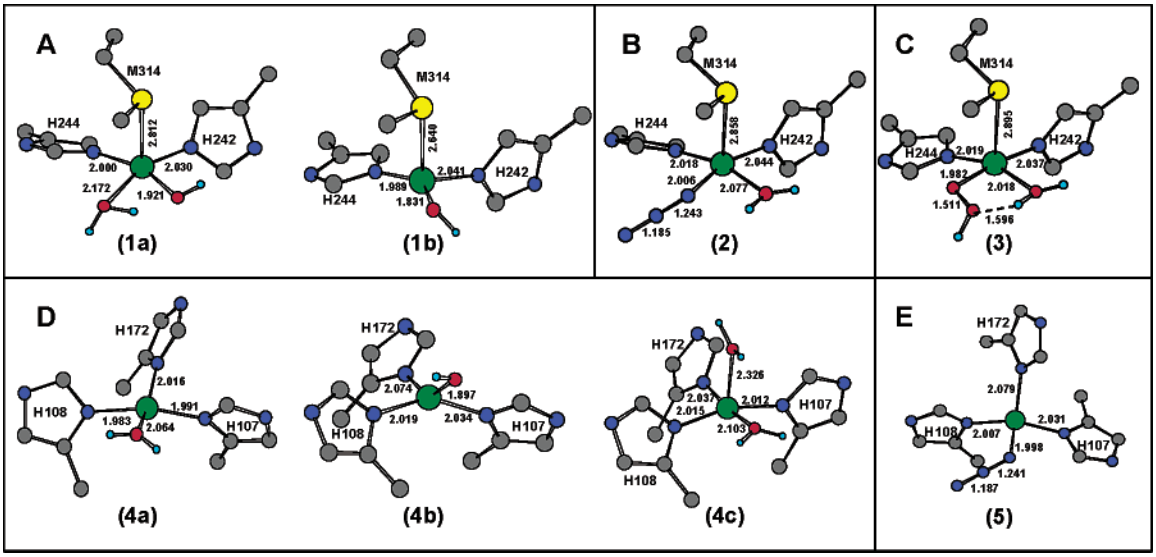

FIGURE 4: Energy-optimized structures of the resting oxidized Cu_M (A), the N_3^--bound form, Cu^{II}_M−N_3^- (B), the putative hydroperoxo intermediate, Cu^{II}_M−OOH (C), the resting oxidized Cu_H (D), and the N_3^--bound form, Cu^{II}_H−N_3^- (E). Relevant bond lengths (Å) are labeled on the structures. Hydrogen atoms on the histidine and methionine ligands are omitted for clarity. Color codes are as follows: Cu, green; N, blue; C, gray; O, red; S, yellow; H, light blue.

MCD pseudo-*A*-term, very similar to the pseudo-*A*-term feature observed in the resting PHMcc MCD spectrum (Figure 1A). Similar spectral features are also observed in the MCD spectrum of the model complex $[Cu^{II}(Im)_4](SO_4)$, which has a similar geometric structure to $[Cu^{II}(1,2\text{-dmIm})_4](BF_4)_2$ but with shorter axial metal−anion distances. (Figure S3).

2.2. Geometry Optimized Structures. To quantitatively correlate with the above spectroscopic data, geometric structure information for the Cu sites in PHM is required. Although past studies with X-ray absorption spectroscopy (XAS) (*20*) and crystallographic characterizations (*13*, *17*) have provided consistent descriptions on the geometric structure of the Cu_H site in oxidized PHM, the protonation state of the bound water-derived ligand is not clear. For the Cu_M site, there is some controversy in the literature. While the crystal structure shows that the resting oxidized Cu_M site has a four-coordinate tetrahedral geometry (*17*), spectroscopic data (mainly EPR, XAS, and EXAFS) suggest a five-coordinate square pyramidal geometry with Met314 being the axial ligand (*18*, *20*, *40*). Further, no structural information is available for the N_3^- (i.e., peroxide analogue)-bound form of the PHM Cu sites or the putative Cu^{II}_M−OOH intermediate. In this section, we computationally evaluate possible Cu_M and Cu_H structural models using DFT methods to provide additional structural information for correlation with our spectroscopic results, and evaluation of existing structural models (Analysis section).

2.2.1. The Resting Cu Sites. The PHM Cu_M site has three protein ligands, Met314, His242, and His244 (*13*, *17*). Including the possibilities of one to two water-derived ligands, four structural models were considered and geometry-optimized: $[Cu^{II}_M(Met)(His)_2(H_2O)(OH)]^+$, $[Cu^{II}_M(Met)(His)_2(H_2O)_2]^{2+}$, $[Cu^{II}_M(Met)(His)_2(H_2O)]^{2+}$, and $[Cu^{II}_M(Met)(His)_2(OH)]^+$. The crystal structure coordinates were used as the starting geometries (*13*, *17*). The methionine and histidines were modeled as ethylmethylthioether and methylimidazoles. The α-carbon positions of the methionine/histidine ligands were fixed in space during optimization to mimic the constraining effects of the protein backbone. (In very few cases, one small imaginary frequency (approximately -10 cm^{-1}) is present in the frequency calculations on the optimized structures due to these constraints. The corresponding vibrational modes involve dominantly motions of the α-carbons.) Without fixing the α-carbon positions, geometry optimizations resulted in different structures indicating the importance of incorporating the protein backbone effect on Cu active site geometries. The energy-optimized structures of the $[Cu^{II}_M(Met)(His)_2(H_2O)_2]^{2+}$ and $[Cu^{II}_M(Met)(His)_2(H_2O)]^{2+}$ models show a distorted square pyramidal and a slightly D_{2d} distorted square planar geometry, respectively (Figure S4, parts A and B), both of which have the methionine as one of the equatorial ligands. This is not consistent with previous EXAFS results (*20*, *40*), and the fact that no methionine to Cu^{II} CT transition is present in the absorption spectrum indicates that the methionine has to coordinate at an axial position. These two models were thus eliminated from further evaluation. The $[Cu^{II}_M(Met)(His)_2(H_2O)(OH)]^+$ model has a square pyramidal geometry in the optimized structure with a long axial Cu−methionine bond (∼2.81 Å) and two histidines, H_2O, and OH^- as the four equatorial ligands (**1a** in Figure 4A). The average equatorial metal−ligand bond length is ∼2.03 Å. The structure is consistent with the proposed Cu_M structural model based on spectroscopic studies (*20*). The geometry-optimized $[Cu^{II}_M(Met)(His)_2(OH)]^+$ model could be described as either a trigonally distorted tetrahedral structure with methionine at the axial position or a distorted tetragonal structure with an open equatorial position opposite to His242 (**1b** in Figure 4A). The Cu−methionine bond is ∼2.62 Å, and the average equatorial metal−ligand bond length is about 1.95 Å. This structure is consistent with the geometric description from the PHMcc crystal structure (*17*).

Parallel geometry optimizations were also performed on the possible models for the resting oxidized Cu_H site, which has three histidine ligands from the protein backbone. Four structural models were evaluated with one or two water-derived ligands: $[Cu^{II}_H(His)_3(H_2O)]^{2+}$, $[Cu^{II}_H(His)_3(OH)]^+$,

$[Cu^{II}_H(His)_3(H_2O)_2]^{2+}$, and $[Cu^{II}_H(His)_3(H_2O)(OH)]^+$. The $[Cu^{II}_H(His)_3(H_2O)(OH)]^+$ model is not a stable structure, and the H_2O ligand dissociates from the Cu center. This model can thus be eliminated. The optimized structures of the other three models are shown in Figure 4D. The optimized $[Cu^{II}_H(His)_3(H_2O)]^{2+}$ model (**4a**) has a square planar geometry with a slight D_{2d} distortion. The $[Cu^{II}_H(His)_3(OH)]^+$ model (**4b**) has a D_{2d} distorted tetrahedral structure. The $[Cu^{II}_H(His)_3(H_2O)_2]^{2+}$ model (**4c**) has a square pyramidal geometry with a long axial Cu−H_2O bond ($r_{Cu-O,ax} \approx 2.33$ Å). The average equatorial metal−ligand bond lengths are about 2.01, 2.01, and 2.04 Å for **4a**, **4b**, and **4c**, respectively (Figure 4D). These three resting oxidized Cu_H model structures are all consistent with the PHMcc crystal structures (*17*), although structures **4a** and **4b** agree better with the previous spectroscopically defined tetragonal geometric description (*20*) since structure **4c** is distorted toward a tetrahedral geometry. The possible structural models for the resting oxidized Cu_M and Cu_H sites (**1a**, **1b**, **4a**, **4b**, and **4c**) will be further evaluated on the basis of our spectroscopic results in the Analysis section.

2.2.2. The N_3^--Bound Forms and the Putative Cu^{II}_M−OOH Intermediate. Possible structural models of the N_3^--bound forms of the PHM Cu sites were also calculated and geometry-optimized for correlation with our spectroscopic results. Only two structural models are stable for the N_3^--bound Cu_M site, $[Cu^{II}_M(Met)(His)_2(H_2O)(N_3)]^+$ (**2** in Figure 4B) and $[Cu^{II}_M(Met)(His)_2(N_3)]^+$ (Figure S4C). The $[Cu^{II}_M(Met)(His)_2(N_3)]^+$ model structure is very tetrahedral and could be eliminated on the basis of the spectroscopic features of N_3^--bound PHMcc (vide infra). The optimized structure of the $[Cu^{II}_M(Met)(His)_2(H_2O)(N_3)]^+$ model (**2**) has a square pyramidal geometry with the Met-S being the axial ligand ($r_{Cu-S} \approx 2.86$ Å), and the N_3^- is bound equatorially in an end-on fashion (average equatorial $r_{metal-ligand} \approx 2.04$ Å, Figure 4B). (The model structure $[Cu^{II}_M(Met)(His)_2(OH)(N_3)]$, where the bound H_2O at the resting Cu^{II}_M site is replaced by N_3^-, is not stable during geometry optimization and leads to dissociation of the methionine ligand.) The only stable structure optimized for the N_3^--bound Cu_H site is the $[Cu^{II}_H(His)_3(N_3)]^+$ model (**5**, Figure 4E). It has a D_{2d} distorted square planar geometry where the N_3^- ligand binds terminally (average $r_{metal-ligand} \approx 2.03$ Å). In both N_3^--bound structures **2** and **5**, the N−N bond lengths are inequivalent with the remote N−N bond being ∼0.05 Å shorter than the proximal one (Figure 4B,E). This is consistent with previous studies of N_3^- bound terminally to Cu^{II} centers, which showed that the $N^2-N^+\equiv N$ resonance structure of the N_3^- molecule is stabilized relative to the $N^-=N^+=N^-$ structure upon binding to metal centers (*21*).

The N_3^- ligand is a reasonable spectroscopic and electronic structure analogue of hydroperoxide because both have low-lying occupied π orbitals (π^* in hydroperoxide, π^{nb} in N_3^-) that dominate the donor bonds (*21, 22*). Therefore, the geometry of the N_3^--bound Cu_M model (**2**) was used as the starting structure for geometry optimization of the widely proposed Cu^{II}_M−OOH intermediate by substituting the end-on bound N_3^- with the HOO^- ligand. The final optimized structure of the $[Cu^{II}_M(Met)(His)_2(H_2O)(OOH)]^+$ model (**3**) is shown in Figure 4C. It has a square pyramidal geometry with Met-S as the axial ligand ($r_{Cu-S} \approx 2.90$ Å) and the hydroperoxide bound equatorially in an end-on fashion and hydrogen-bonded to the coordinated H_2O (average equatorial $r_{metal-ligand} \approx 2.01$ Å).

Scheme 1: Schematic Ligand Field State Energy Diagram for the Tetrakisimidazole Cu^{II} Complex and Absorption and MCD Selection Rules[a]

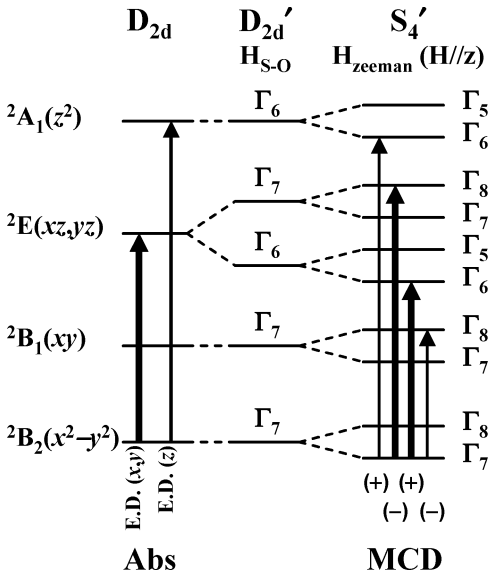

[a] The *x* and *y* axes defined here are approximately along the metal−ligand bonds in the tetrakisimidazole Cu^{II} complexes and are 45° rotated (around *z*) from the conventional axis definition in the D_{2d} point group to make the $d_{x^2-y^2}$ orbital highest in energy among the five d orbitals. The orbital label in parentheses indicates the location of the d hole of the Cu^{II} center. The thickness of the arrows indicates the relative transition intensity. The absorption polarizations and MCD signal signs are indicated below the transition arrows.

3. ANALYSIS

3.1. Ligand Field Analysis. 3.1.1. MCD Selection Rules and Spectral Assignments. In this section, we focus on the crystallographically defined $[Cu^{II}(1,2\text{-dmIm})_4]^{2+}$ model complex to obtain ligand field absorption/MCD selection rules and make spectral assignments for correlation with the protein data. The CuN_4 core of the $[Cu^{II}(1,2\text{-dmIm})_4]^{2+}$ complex has a slight D_{2d} distortion from idealized D_{4h} symmetry (*24*). This removes the inversion center of the molecule increasing the intensity of ligand field, d−d, transitions, which would otherwise be parity forbidden. The ligand field state energy diagram for a Cu^{II} complex with $D_{2d}(D_{4h})$ symmetry is shown in Scheme 1 (left column). There are three ligand field excited states, $^2B_1(xy)$, $^2E(xz,yz)$ (doubly degenerate), and $^2A_1(z^2)$ (*41*). The ground state is $^2B_2(x^2-y^2)$. Two transitions are electric dipole (ED) allowed in absorption. The transition to the doubly degenerate $^2E(xz,yz)$ excited state is polarized along the *x* and *y* directions. The transition to the $^2A_1(z^2)$ state is allowed in the *z* direction. The $^2B_2(x^2-y^2) \rightarrow {}^2E(xz,yz)$ transition should be more intense in absorption as it gains intensity through configuration interaction with higher energy equatorial ligand to Cu CT transitions, which are also *x,y* polarized. The higher CT intensity derives from the large orbital overlap between the ligand donor and the Cu x^2-y^2 acceptor orbital (Scheme 1, left column). Spin−orbit coupling within the $^2E(xz,yz)$ state splits the degenerate pair in energy (by $|\lambda|$, ∼830 cm^{-1} for Cu^{II}) into two states that transform as Γ_6 ($|m_J| = {}^1/_2$) and Γ_7 ($|m_J| = {}^3/_2$) in the D_{2d}' double group (Scheme 1, center

column) (*42*). The ground state $^2B_2(x^2-y^2)$ transforms as Γ_7 with $|m_J| = {}^1/_2$. Application of an axial magnetic field removes all spin degeneracy and lowers the effective symmetry to S_4' (*42*). The splitting of the ligand field states due to the magnetic field is summarized in Scheme 1, right column. The lowest energy state is the $m_J = -{}^1/_2$ component of the ground Kramers doublet and transforms as Γ_7 in the S_4' double group. This component is the most populated in the low-temperature condition of the MCD experiment. MCD measures the absorption difference between left and right circularly polarized light ($\Delta A = A_{left} - A_{right}$) in a longitudinal magnetic field (*43*). The electric dipole operators for left and right circularly polarized light are $\mathbf{m}_{-1}$ ($= (\mathbf{m}_x - i\mathbf{m}_y)/\sqrt{2}$) and $\mathbf{m}_{+1}$ ($= -(\mathbf{m}_x + i\mathbf{m}_y)/\sqrt{2}$), which transform as Γ_3 and Γ_4, respectively, in the S_4' double group. Therefore, from the Γ_7 component of the ground state, MCD transitions to the Γ_6 and Γ_8 excited states are left (positive, $\Gamma_7\Gamma_3(m_{-1}) = \Gamma_6$) and right (negative, $\Gamma_7\Gamma_4(m_{+1}) = \Gamma_8$) circularly polarized, respectively (Scheme 1, right column). The MCD selection rule requires a transition to have two perpendicular nonzero electric dipole transition moments to have *C*-term intensity (*44*). Thus, only the transitions to the Γ_6 and Γ_8 components of the doubly degenerate $^2E(xz,yz)$ excited state will have significant intensity in the MCD spectrum. These two transitions are close in energy (split by $|\lambda| \approx 830$ cm^{-1}) and opposite in sign, predicting a dominant pseudo-*A*-term spectral feature in the MCD spectrum (Scheme 1, right column). The transitions to the Γ_6 component of the $^2A_1(z^2)$ state and the Γ_8 component of the $^2B_1(xy)$ state spin−orbit couple with the same symmetry components of the $^2E(xz,yz)$ state borrowing nonzero MCD intensity of the same sign (Scheme 1, right column).

The experimentally observed LF transitions in the absorption spectrum of the $[Cu^{II}(1,2\text{-dmIm})_4](BF_4)_2$ complex at 15 000−20 000 cm^{-1} are low in intensity with extinction coefficients around 50−100 M^{-1} cm^{-1} (Figure 3A and section 2.1). Their energies are typical for Cu^{II} complexes in a close to square planar geometry (*45*). The strongest absorption band at ∼19 000 cm^{-1} can be assigned as the $^2B(x^2-y^2) \rightarrow {}^2E(xz,yz)$ transition (Figure 3A, Scheme 1, left column). The two MCD transitions at ∼17 000 (+) and ∼19 500 (−) cm^{-1}, which form the dominant pseudo-*A* term in the MCD spectrum, can be assigned as the two spin-orbit split components, $^2\Gamma_6(xz/yz)$ and $^2\Gamma_8(xz/yz)$, of the $^2E(xz,yz)$ state, respectively (Figure 3B, Scheme 1 right column). The weak negative MCD transition at ∼15 500 cm^{-1} can be assigned as the transition to the $^2\Gamma_8(xy)$ state. Its corresponding absorption transition ($^2B_1(xy)$) appears as a shoulder at ∼16 000 cm^{-1} (Figure 3A). The higher energy positive MCD feature at ∼23 000 cm^{-1} can be assigned as the transition to the $^2\Gamma_6(z^2)$ state; its corresponding absorption feature is not experimentally resolved (Figure 3A,B). Similar spectral assignments can be applied to the absorption/MCD spectra of the $[Cu^{II}(Im)_4](SO_4)$ complex (Figure S3). The positive $^2\Gamma_6(z^2)$ transition is not observed in the MCD spectrum (Figure S3B). This is likely due to additional axial interactions with the sulfate ligand relative to $[Cu^{II}(1,2\text{-dmIm})_4](BF_4)_2$ (Figure S1B), which would decrease the $^2\Gamma_6(z^2)$ state transition energy and result in its overlap with the *xz*/*yz* transitions, which are dominant in MCD.

The dominant pseudo-*A*-term feature in the MCD spectrum of resting PHMcc can be assigned as the Cu^{II} ligand field x^2-y^2 to *xz*/*yz*, $^2B_1 \rightarrow {}^2E$, transitions, on the basis of the overall spectral similarity to the model complexes (Figures 1A, 3B, and S2B). The negative MCD Cu^{II} *xy* transition is not resolved for resting PHMcc, which could be due to its low intensity (Figures 3B and S2B) and the lower signal/noise ratio of the protein spectrum. The positive MCD Cu^{II} $x^2-y^2 \rightarrow z^2$ transition is also not observed. This suggests possible axial interactions at the protein Cu^{II} sites, which could lower the z^2 transition energy and result in its overlap with the strong *xz*/*yz* transitions, as in the case of the $[Cu^{II}(Im)_4](SO_4)$ model (Figure S3B). Importantly, only one set of Cu^{II} *xz*/*yz* transitions are observed in the resting PHMcc MCD spectrum, while there are two inequivalent protein Cu sites (Cu_M and Cu_H). This suggests that these two Cu^{II} sites have very similar d orbital splittings from their ligand field geometries. This is evaluated below.

Table 2: Ligand Field Parameters

ligand	*r* (Å)	α_2 (cm^{-1})	α_4 (cm^{-1})	ligand	*r* (Å)	α_2 (cm^{-1})	α_4 (cm^{-1})
Reference Model				$Cu^{II}_H(His)_3(H_2O)$ (**4a**)			
Im[a]	2.031	12032	4462	His	1.991	12772	4929
H_2O[b]	2.019	17269	6540		1.983	12927	5029
	2.230	12814	1798		2.016	12303	4630
OH^- [c]	1.918	16000	13000	H_2O	2.064	16164	5857
Met-S[d]	2.30	13400	6700				
	2.90	4000	1000				
$Cu^{II}_M(His)_2(Met)(H_2O)(OH)$ (**1a**)				$Cu^{II}_H(His)_3(OH)$ (**4b**)			
His	2.030	12050	4473	His	2.034	11979	4429
	2.000	12600	4819		2.019	12248	4596
Met-S	2.812	4387	1167		2.074	11299	4018
H_2O	2.172	13868	2051	OH^-	1.897	16537	13736
OH^-	1.921	15925	12899				
$Cu^{II}_M(His)_2(Met)(OH)$ (**1b**)				$Cu^{II}_H(His)_3(H_2O)_2$ (**4c**)			
His	2.041	11856	4354	His	2.012	12376	4677
	1.989	12810	4953		2.015	12321	4642
Met-S[e]	2.640	8073	3470		2.037	11926	4397
OH^-	1.831	18391	16396	H_2O	2.103	15281	5334
					2.326	11292	1456

[a] Ligand field fit to hexakis(imidazole)copper(II) nitrate complex (Table S2) (*47*). [b] Ligand field fit to hexaaquocopper(II) complex (Table S3) (*48, 49*). [c] Ligand field fit to $[Cu^{II}(OH)\{HB(3\text{-}t\text{Bu-}5\text{-}i\text{Prpz})_3\}]$ complex (Table S4) (*16, 50*). [d] From ref *46*. [e] Because of the large Cu−S bond length difference with the two reference Cu−S bond lengths, the parameters here are obtained by linear extrapolations between the two sets of model reference values.

3.1.2. Ligand Field Calculations. The DFT-optimized structures of possible Cu_M and Cu_H site models can be used to calculate their LF energy levels using the approach developed by Companion and Komarynsky (*32*) and applied to bioinorganic Cu^{II} and Fe^{II} sites (*32, 44, 46*). The ligands are treated as point charges, which perturb the Cu^{II} d orbitals due to electrostatic interactions based on the geometric arrangement of the ligands around the metal. The interactions of each ligand with the metal are parametrized by radial integrals α_2 and α_4 (*32*), which are obtained experimentally through fitting LF data on model complexes with defined geometries. The α_2 and α_4 parameters obtained in this way for imidazole, H_2O, OH^-, and Met-S ligands are given in Table 2 with corresponding Cu−ligand bond lengths. Individual ligand parameters for each DFT-optimized Cu_M and Cu_H models were scaled from the reference model values using the approximation that α_2 and α_4 are proportional to $1/r^3$ and $1/r^5$, respectively, where *r* is the metal−ligand bond length (Table 2). (For cases where two model reference

Table 3: Ligand Field Calculated d−d Transition Energies, EPR *g* Values, and Stevens' Orbital Reduction Factor

structures	*xy*	*xz*/*yz*	z^2	*xz*/*yz*	g_x	g_y	g_z	$\Delta g_\perp$	$k_\perp^{2\,c}$	$k_\parallel^2$	β^2
PHMcc experimental[a]		12000−15500		16600−16700	2.050	2.060	2.288	0.01			0.70
1a $Cu^{II}_M(His)_2(Met)(H_2O)(OH)$	8633	15366	15125	17143	2.035	2.075	2.288	0.04	0.52	0.38	0.64[b]
1b	8576	11583	13624	15749	2.003	2.107	2.288	0.10	0.29	0.48	0.54[b]
4a $Cu^{II}_H(His)_3(H_2O)$	7906	15339	16851	16728	2.049	2.061	2.288	0.01	0.52	0.34	0.64[b]
4b	9244	12832	15660	13953	2.041	2.069	2.288	0.03	0.44	0.41	0.58[b]
4c	7687	11768	10088	12597	2.036	2.074	2.288	0.04	0.37	0.33	0.67[b]

[a] The experimental transition energies were obtained through Gaussian resolution of the resting PHMcc MCD spectrum (Figure 1A). The absolute peak positions could not be determined accurately due to the derivative spectral shape where the positive and negative parts could cancel each other. The spectrum was thus fitted with two bands while varying their energy splitting. The energy range reported here is maximally allowed values without significantly deteriorating the fit quality. The higher energy *xz*/*yz* transition is quite accurate due to its much larger intensity relative to the lower energy component. The *g* and β^2 values are from Table 1. [b] DFT-calculated ground-state Cu covalency. [c] $k_\perp^2$ was determined by scaling the average value of LF calculated g_x and g_y (before correction) to the average value of the experimental g_x and g_y values.

values are available, the value associated with the bond length closest to the DFT-calculated one is used.) The α_2 and α_4 values for the histidine (imidazole), H_2O, and OH^- ligands should be reasonable because the differences between the bond lengths in the calculated Cu_M/Cu_H structures and those in the reference model systems are very small. The Met-S LF parameter values should also be reasonable because the Cu−S bond length in structure **1a** is very close to that of the reference model complex, while the α_2 and α_4 values for Met-S in structure **1b** ($r_{Cu-S} = 2.64$ Å) are bounded by the values of two model complexes with Cu−S distances of 2.30 and 2.90 Å.

The d−d transition energies obtained from the LF calculations on the DFT-optimized Cu_M and Cu_H model structures are given in Table 3 and compared with the experimental data. The *g* values were also calculated using the LF-derived eigenfunctions and the perturbative approach outlined by Ballhausen (*46*, *51*) and further corrected using Stevens' orbital reduction factors to account for ligand covalency.

For the structural models of the PHM Cu_M site (Figure 4A), structure **1a** gives better agreement with both *xz*/*yz* transitions than structure **1b,** which underestimates their energies (Table 3). The predicted *xz*/*yz* energy splitting is quite large for structure **1b** (∼4200 cm^{-1}) relative to that of structure **1a** (∼1800 cm^{-1}) and experiment (∼2900 cm^{-1}). The LF calculated *g* values for structure **1b** show a significant rhombic splitting ($\Delta g_\perp = 0.10$), which is not consistent with the experimentally observed axial EPR pattern of PHM. The large LF *xz*/*yz* splitting and rhombic *g* values of structure **1b** result from its ligand field, which is more appropriately described as a distorted tetragonal structure with an open equatorial site (Figure 4A, section 2.2.1). The vacant equatorial position leads to a large inequivalence in the *x* and *y* directions giving the large *xz*/*yz* splitting, while the overall distorted structure results in a significant z^2 mixing into the x^2-y^2 ground state (∼19% from the LF calculation), which is the dominant factor leading to the rhombic EPR pattern. (DFT-calculated ground-state wave function for structure **1b** (see section 3.2 and Figure S5A) gives ∼4% z^2 mixing in the ground state, which corresponds to a rhombic splitting ($\Delta g_\perp$) of ∼0.1 (*36*).) Therefore, the LF analysis indicates that the most reasonable Cu_M structural model is $[Cu^{II}_M(His)_2(Met)(H_2O)(OH)]^+$ (**1a**, Figure 4A), which is square pyramidal with the Met-S as the axial ligand. This is consistent with the previous Cu_M structural model based on XAS data (*20*). The DFT-optimized structure **1a** provides a detailed model for Cu_M based on spectroscopy.

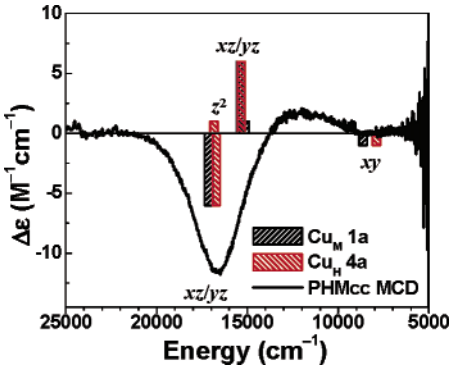

FIGURE 5: Predicted d−d transition energies from ligand field calculations overlaid on the resting PHMcc MCD spectrum. The sizes of the bars indicate the predicted relative transition intensities with appropriate signal signs (see Scheme 1).

For the structural models of the PHM Cu_H site (Figure 4D), LF calculations on structure **4c** underestimate the energies of both *xz*/*yz* LF transitions, particularly the higher-energy component, which is underestimated by ∼4000 cm^{-1} (Table 3). Structure **4c** can thus be eliminated. The results on structure **4b** give good agreement for the low-energy component of the *xz*/*yz* transitions, while the higher-energy component is underestimated by ∼2600 cm^{-1} (Table 3), arguing against structure **4b** for the Cu_H site. The LF results from structure **4a** are in best agreement with experiment (Table 3). Therefore, the $[Cu^{II}_H(His)_3(H_2O)]^{2+}$ structure (**4a** in Figure 4D) is a reasonable model for the PHM Cu_H site, where the Cu^{II} center has a D_{2d} distorted square planar geometry. This is consistent with the previously described Cu_H structure based on both spectroscopy and crystallography (*17*, *20*).

The LF calculated d−d transitions of structures **1a** (Cu_M) and **4a** (Cu_H) are plotted on the resting PHMcc MCD spectrum in Figure 5. The similarity between the d−d transition energies of the Cu_M and Cu_H sites is clearly demonstrated, especially for the two intense *xz*/*yz* transitions. This is consistent with the spectroscopic data that show only one set of *xz*/*yz* transitions forming the dominant pseudo-*A* term in the MCD spectrum of resting PHMcc. This appears to be inconsistent with the fact that there are two inequivalent Cu sites in the protein (Figure 1A), and the PHMcc + NO_2^- data show that both sites contribute to the MCD spectrum (Figure 1E). The z^2 transitions for both Cu sites are located in the region of the strong negative MCD feature of the pseudo-*A* term and are thus not resolved experimentally. Further correlations between the Cu_M **1a** and Cu_H **4a** ligand field will be discussed in section 4.

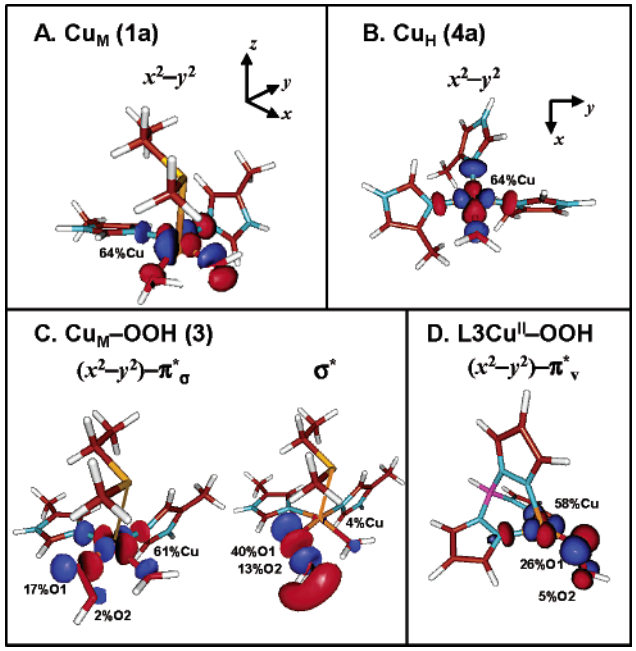

FIGURE 6: Surface contour plots of DFT-calculated spin-down LUMOs of Cu_M **1a** (A), Cu_H **4a** (B), and Cu^{II}_M−OOH **3** (C) structures. The spin-down σ^* orbital of Cu^{II}_M−OOH is also shown in panel C. Molecular coordinate systems used here are shown for Cu_M and Cu_H sites in panels A and B. Panel D shows a surface contour plot of the spin-down LUMO of the L3Cu^{II}−OOH model complex (L3 = [HB(3-*t*Bu-5-*i*Prpz)$_3$]), adapted from ref *16*. Relevant MO decompositions are labeled in percentages.

The spectroscopically defined Cu_M **1a** and Cu_H **4a** structures also provide a rationale for the fact that these two sites could be spectroscopically differentiated upon binding NO_2^- (Figure 1E,F, section 2.1). The Cu_M site (**1a**) has two equatorial water-derived ligands that are exchangeable, while the Cu_H site (**4a**) has only one exchangeable equatorial water. Copper model studies have shown that NO_2^- can bind either bidentate through the two terminal oxygen atoms when there are two open equatorial positions (*52*−*54*) or monodentate through one oxygen atom if there is only one open equatorial position (*55*, *56*). Thus NO_2^- binding can differentially perturb the Cu_M and Cu_H centers in PHM, making both sites spectroscopically observable and distinguishable in the MCD and EPR spectra (Figure 1E,F).

3.2. Resting Site Ground-State Wave Function. Surface contour plots of DFT-calculated spin-down LUMOs on the Cu_M **1a** and Cu_H **4a** structures are shown in Figure 6A,B. Because these are all $S = {}^1/_2$ systems, the spin-down LUMOs represent the ground-state wave functions of the resting Cu^{II}_M and Cu^{II}_H sites. Both Cu_M **1a** and Cu_H **4a** have a x^2-y^2 ground state, consistent with the EPR results of resting PHMcc (Figure 1B). The x^2-y^2 orbital of Cu_M **1a** has dominant σ interactions with all four equatorial ligands (two histidines, H_2O, and OH^-, Figure 6A). The Met-S is in the axial position with virtually no contribution in the ground-state wave function indicating that the Cu−methionine interaction is very weak. This is consistent with the long axial Cu−methionine bond ($r \approx 2.8$ Å, Figure 4A) and the fact that no methionine interaction is detected in the EXAFS of resting PHMcc (*18*, *20*). The x^2-y^2 orbital of Cu_H **4a** has dominant σ interactions with the four equatorial ligands (three histidines and H_2O, Figure 6B), similar to that of Cu_M **1a**. The ground-state Cu covalencies for Cu_M **1a** and Cu_H **4a** are calculated to be very similar, about ∼64% Cu character, more covalent than the experimental value determined from EPR (∼70% Cu, Table 1). This agrees with past studies that the B3LYP functional overestimates ground-state covalencies of Cu^{II} complexes (*57*). The important point here is that the ground-state Cu covalencies of the Cu_M **1a** and Cu_H **4a** sites are essentially equal. Together with their similar LF transition energies, both the Cu_M and Cu_H sites should exhibit very similar EPR *g* and *A* values, since the *g* values are only dependent on LF energies and covalencies and the *A* values depend on the *g* values and covalency of the ground state. This is indeed reflected experimentally in the EPR spectrum of resting PHMcc where only one Cu^{II} EPR signal is observed (Figure 1B).

3.3. Electronic Structure Description of the Putative Cu^{II}_M−OOH Intermediate. 3.3.1. N_3^--Bound PHM. N_3^- was used as a spectroscopic and electronic analogue of OOH^- to probe the Cu sites in resting PHMcc. The EPR spectrum of PHMcc + N_3^- shows one type of tetragonal Cu EPR signal, similar to that of resting PHMcc but with a smaller g_z value, indicating that *both* Cu sites in the protein are perturbed (Figure 1D, Table 1, section 2.1). Two intense (and one weak) CT transitions are observed in the absorption spectrum of PHMcc + N_3^- at 25 550 cm^{-1} ($\epsilon \approx 2550$ M^{-1} cm^{-1}) and 29 600 cm^{-1} ($\epsilon \approx 2100$ $M^{-1}cm^{-1}$) with two corresponding negative bands in the MCD spectrum (Figure 2). The absorption intensities of these two CT transitions require significant overlap between N_3^- π^{nb}_σ and Cu x^2-y^2 orbitals (*21*). N_3^- thus must bind equatorially to the Cu sites, one to each Cu site, since one N_3^- molecule can only contribute to one intense CT absorption transition. The DFT-optimized structures Cu^{II}_M−N_3^- **2** (Figure 4B) and Cu^{II}_H−N_3^- **5** (Figure 4E) are consistent with the spectroscopic results; both have one equatorial N_3^- bound to the Cu centers. Specifically, the higher energy transition at 29 600 cm^{-1} can be associated with the N_3^- $\pi^{nb}_\sigma \rightarrow Cu^{II}_M$ x^2-y^2 transition, while the lower energy transition can be assigned to the N_3^- $\pi^{nb}_\sigma \rightarrow Cu^{II}_H$ x^2-y^2 transition. The energy difference comes from their difference in Cu coordination numbers (Cu^{II}_M−N_3^- **2**, five-coordinate; Cu^{II}_H−N_3^- **5**, four-coordinate; Figure 4B,E) where the higher coordination number leads to the higher energy CT transition due to the shift in the Cu d manifold to higher energy from more ligand repulsion and a lower Cu effective nuclear charge (Z_{eff}). In correlation to the NO_2^- binding studies (Section 2.1), the inequivalent energies of the two N_3^- $\pi^{nb}_\sigma \rightarrow$ Cu CT bands observed experimentally provide further support for the inequivalence of the Cu_M and Cu_H sites. The CT band at 21 950 cm^{-1} with low intensity ($\epsilon \approx 1050$ $M^{-1}cm^{-1}$) can be associated with the N_3^- $\pi^{nb}_v \rightarrow$ Cu transition of one Cu site. The N_3^- π^{nb}_v orbital is perpendicular to the Cu x^2-y^2 orbital with little orbital overlap and thus low in intensity.

The Cu LF *xz*/*yz* transitions in the MCD spectra are only slightly perturbed by N_3^- binding to PHMcc (Figure 1A,C), indicating that the Cu site geometries in the N_3^--bound form remain tetragonal and similar to resting PHMcc. This is consistent with the DFT-optimized structures Cu^{II}_M−N_3^- **2** and Cu^{II}_H−N_3^- **5** (Figure 4B,E), which have square pyramidal and D_{2d} distorted square planar geometries, respectively, paralleling the resting Cu_M **1a** and Cu_H **4a** structures (Figure 4A,D). The LF data of PHMcc + N_3^- also rule out

the other computationally stable structure ($[Cu^{II}_M(Met)(His)_2(N_3)]^+$, Figure S4C) because it has a close to tetrahedral geometry.

3.3.2. Electronic Structure of the Putative Cu^{II}_M−OOH Intermediate. The DFT-optimized structure **3** for the putative Cu^{II}_M−OOH intermediate has a square pyramidal geometry (Figure 4C). This is very similar to the spectroscopically defined Cu^{II}_M−N_3^- structure **2**, which was used as the starting geometry with substitution of the N_3^- by OOH^-, reflecting the electronic analogy between N_3^- and OOH^-. The OOH^- binds in an end-on fashion to the Cu^{II} center. (The deprotonated water ligand form of Cu^{II}_M−OOH **3**, $[Cu^{II}_M(Met)(His)_2(OH)(OOH)]$, was also geometry-optimized and found to be ∼25 kcal/mol higher in free energy.) The ground-state wave function of this Cu^{II}_M−OOH **3** intermediate is shown in Figure 6C, left, and consists mainly of the Cu x^2-y^2 orbital, similar to that of resting Cu_M **1a** (labeled $(x^2-y^2)-\pi^*_\sigma$, Figure 6A). The OOH^- π^*_σ orbital is in the Cu−O−O plane and forms a dominant but not very covalent pseudo-σ interaction with the Cu^{II} x^2-y^2 orbital, since there is only a total of 19% OOH^- character in the wave function. The OOH^- π^*_σ component of the ground-state wave function is highly polarized toward the Cu (ligating oxygen, ∼17%; remote oxygen, ∼2%), similar to the behavior observed in Cu^{II}−OOH model complexes (*16*, *58*). This polarization is mainly due to the effect of protonation and leads to a strengthened O−O bond (*16*, *58*). The OOH^- σ^* orbital (Figure 6C, right) is high in energy (∼3 eV higher than the spin-down LUMO) and also polarized toward the Cu (ligating oxygen, ∼40%; remote oxygen, 13%), similar to that of Cu^{II}−OOH model complexes (*16*, *58*). Possible electronic structure contributions of this putative Cu^{II}_M−OOH **3** intermediate to reactivity will be evaluated below.

4. DISCUSSION

A combination of spectroscopic characterizations and DFT calculations has defined the geometric and electronic structures of the Cu_M and Cu_H sites in resting PHM. The Cu_M site has a square pyramidal geometry with a long axial Cu−methionine bond and two histidines, H_2O, and OH^- as the equatorial ligands (structure **1a**, Figure 4A). The Cu_H site has a slightly D_{2d} distorted square planar geometry with three histidines and H_2O as the equatorial ligands (structure **4a**, Figure 4D). These two sites have very similar ligand field transition energies and ground-state covalencies leading to their indistinguishable contributions in optical and EPR spectra (Figures 1A,B and 6A,B). These spectroscopic properties are the result of the metal−ligand interactions at these LF geometries. The spectral similarities of Cu_M and Cu_H appear to contradict the fact that these two sites have different number and type of ligands; relative to the Cu_H site, the Cu_M site has an additional axial Met-S ligand and an equatorial OH^- in place of a histidine. We have thus performed a LF analysis for a series of intermediate structures correlating the Cu_M and Cu_H sites.

Figure 7 (left) presents the d orbital splittings from the LF calculation on Cu_H **4a** (section 3.1.2). The highest energy d orbital is x^2-y^2 with the *xy*, *xz*/*yz*, and z^2 orbitals at decreasing energy, reflecting the close to square planar geometry of the Cu_H site. Figure 7 (**I.S.1**) shows the d orbital splittings of an intermediate structure derived from Cu_M (structure **1a** in Figure 7, right), where the axial methionine ligand is removed, and the OH^- ligand is replaced by a histidine to have the same ligand set as the Cu_H site. (The α_2 and α_4 parameters for the substituted histidine here were taken as the average values of the three histidine ligands of the Cu_H site.) The Cu atom is above the ligand plane in a square pyramidal geometry. This out of plane distortion from planar geometry mainly results in the lowering of the x^2-y^2 orbital and a slight increase of *xz* and *yz* orbital energies, leading to the decreased energy splittings of the x^2-y^2/*xy* and x^2-y^2/(*xz*,*yz*) orbitals. Having an equatorial OH^- ligand instead of a histidine in this intermediate structure mainly elevates the energy of the x^2-y^2 orbital due to the larger donor interaction of OH^- relative to histidine (α_2 and α_4 in Table 2), resulting in increased energy splittings of the x^2-y^2/*xy* and x^2-y^2/(*xz*,*yz*) orbitals (Figure 7, **I.S.2**). The presence of the axial Met-S ligand at the Cu_M site exerts an additional interaction in the *z* direction and shifts the z^2, *xz*, and *yz* orbitals up in energy, while again decreasing the energy splittings of the x^2-y^2/*xy* and x^2-y^2/(*xz*,*yz*) orbitals (Figure 7, right). Thus, the effects of the square pyramidal distortion and addition of the axial methionine ligand at the Cu_M site oppose the effects of the strong donating equatorial OH^- ligand on the Cu d orbital splitting pattern, leading to LF transition energies similar to those of the Cu_H site (Figure 7, left and right, and Figure 5). The only significant difference is the energy of the z^2 orbital, which is higher for the Cu_M site due to the axial Met-S interaction. However, the $z^2 \rightarrow x^2-y^2$ transition does not contribute to the EPR *g* values (for a x^2-y^2 ground state, $g_z = 2.0 - 8\lambda\alpha_1^2\beta_1^2/\Delta E_{xy}$ and $g_{x,y} = 2.0 - 2\lambda\gamma_1^2\beta_1^2/\Delta E_{xz,yz}$, where α_1, β_1, and γ_1 are the Cu *xy*, x^2-y^2, and *xz*/*yz* orbital contributions in the LF wave functions and ΔE_{xy} and $\Delta E_{xz,yz}$ are the *xy* and *xz*/*yz* to x^2-y^2 transition energies (*59*)) and is not observable in the

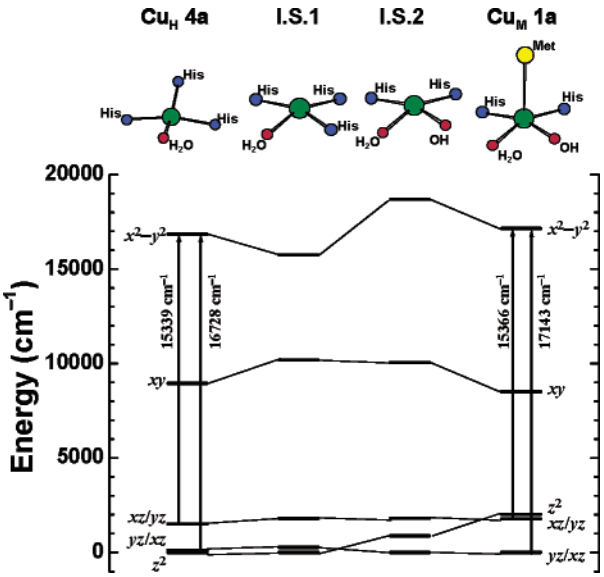

FIGURE 7: Structural correlations of ligand field splitting patterns. Ligand field calculated d−d orbital energy diagrams for Cu_H **4a** (left) and Cu_M **1a** (right). **I.S.1** is an intermediate structural model derived from Cu_M **1a** where the axial methionine is removed and the equatorial OH^- is replaced by a histidine ligand. **I.S.2** is an intermediate structural model with the axial methionine removed from Cu_M **1a**. All energies are referenced to the lowest d orbital, which is set to zero. Geometries of first coordination sphere atoms are shown on the top. Coordinate systems are the same as those defined in Figure 6A,B.

MCD spectrum due to overlap with the dominant pseudo-*A* term associated with the $xz/yz \rightarrow x^2-y^2$ transitions in the MCD spectrum (Figure 5).

Azide binding studies on resting PHM have provided a geometric and electronic structure model for the azide-bound form, $Cu^{II}_M-N_3^-$ (structure **2**, Figure 4B), and facilitated development of a structural model for the putative Cu^{II}_M−OOH species (structure **3**, Figure 4C) previously proposed as a reactive intermediate in catalysis by PHM and DβM (*5, 7, 60*). This Cu^{II}_M−OOH model provides an electronic structure description of the Cu−hydroperoxide and the O−O bonding interactions (section 3.3.2). The π^*_σ orbital of the bound OOH^- ligand forms a dominant pseudo-σ interaction with the Cu^{II}_M x^2-y^2 orbital; the resulting interaction is not very covalent (61% Cu + 19% OOH^-, Figure 6C, left). This bonding description is different from the results on a previously characterized mononuclear $L3Cu^{II}$−OOH model complex (L3 = [HB(3-*t*Bu-5-*i*Prpz)$_3$]) (*16*), where the π^*_v orbital of the OOH^- ligand undergoes a dominant π donor interaction with the Cu^{II} x^2-y^2 orbital, which results in a more covalent Cu−O bond (58% Cu + 31% OOH^-, Figure 6D). The difference in the Cu−O bonding interactions between Cu^{II}_M−OOH and $L3Cu^{II}$−OOH derives from their different LF geometries. The Cu^{II}_M−OOH intermediate is five-coordinate and has a square pyramidal geometry resulting in a Cu x^2-y^2 orbital lobe oriented along the Cu−O bond and thus a pseudo-σ bonding interaction with the OOH^- ligand (Figure 6C, left). The $L3Cu^{II}$−OOH model complex is four-coordinate and has a trigonally distorted tetrahedral geometry where the Cu^{II} x^2-y^2 orbital has two adjacent lobes bisected by the Cu−O bond leading to a π bonding interaction with the OOH^- ligand (Figure 6D). The higher coordination number of the Cu^{II}_M−OOH species raises the energy of the Cu d manifold due to the increased ligand repulsion and lower Z_{eff}, increasing the energy separation between the Cu d and the OOH^- ligand valence orbitals. This results in the less covalent, weaker Cu−O bond in Cu^{II}_M−OOH relative to that of the $L3Cu^{II}$−OOH complex. In contrast to the Cu−O bond, the O−O bond strength in Cu^{II}−hydroperoxide species is mainly determined by the protonation, which increases the bond strength, and is thus not significantly affected by the Cu−O interaction (*16, 58*). The internal H-bond structure feature of the Cu^{II}_M−OOH intermediate **3** (Figure 4C) will contribute to the energetics of its formation (*61*), which is addressed in another study (*62*).

The bonding description of the putative Cu^{II}_M−OOH species provides initial insight into its possible reactivity in the H-atom abstraction reaction, which occurs in PHM and DβM catalysis (*5, 9*−*12*). This would involve the homolytic cleavage of the O−O bond generating a Cu^{II}−oxyl/Cu^{III}−oxo product species. Our previous studies on the $L3Cu^{II}$−OOH model have shown that this reaction is endothermic by ∼45 kcal/mol due to the high-energy product generated, which is best described as a Cu^{II}−oxyl rather than a Cu^{III}−oxo species (*16*). The high Cu^{II}/Cu^{III} redox potential and the inability of the pyrazole ligand to stabilize the Cu^{II}−oxyl species are the main factors contributing to this large ΔE. Comparatively, the Cu^{II}_M−OOH species has a higher coordination number than the $L3Cu^{II}$−OOH complex, which would contribute to stabilizing the Cu^{II}_M−oxyl species through charge donation. However, its less covalent Cu−O interaction would tend to destabilize the product. The equatorial histidine ligands in Cu^{II}_M−OOH are very similar to the pyrazole ligands in $L3Cu^{II}$−OOH in electronic properties (*63*) and would not assist in product stabilization, nor would the bound water ligand, which is an even poorer donor ligand than histidine. (The possibility that the water ligand would deprotonate upon the homolytic O−O bond cleavage and the resulting OH^- ligand would possibly stabilize the Cu^{II}_M−oxyl intermediate is evaluated by DFT geometry optimizations. The methionine ligand dissociates for the Cu^{II}_M−oxyl intermediate with OH^- ligand, and the total energy goes up by >9 kcal/mol relative to the Cu^{II}_M−oxyl intermediate with H_2O ligand.) However, the Cu^{II}_M−OOH species has a Met-S ligand, which is a much better donor ligand and easier to oxidize than the pyrazoles of the $L3Cu^{II}$−OOH complex. Although the Met-S has virtually no contribution to the ground-state wave function of the Cu^{II}_M−OOH species (Figure 6c, left), it may contribute to the stabilization of the Cu^{II}_M−oxyl product upon Cu^{II}_M−OOH H-atom abstraction on substrate. The geometry-optimized structure of the Cu^{II}_M−oxyl species indicates that the Met-S ligand is in fact in an equatorial position and becomes partially oxidized relative to that in the Cu^{II}_M−OOH intermediate, contributing to the stabilization of the Cu^{II}_M−oxyl species (*62*). This Met-S contribution could have significant effects on the energetics of the H-atom abstraction reaction by the Cu^{II}_M−OOH intermediate. The energetics and reaction barrier of Cu^{II}_M−OOH H-atom abstraction are evaluated in another study (*62*), along with another alternative reaction pathway for the PHM reaction.

NOTE ADDED IN PROOF:

A Cu^{II}-superoxide species has recently been proposed to be the reactive Cu/O_2 intermediate for H-atom abstraction in DβM chemistry (*64*). The reaction thermodynamics and energy barriers for the H-atom abstraction reaction of Cu^{II}_M-superoxo and Cu^{II}_M-OOH species in PHM have been evaluated in ref *62*.

SUPPORTING INFORMATION AVAILABLE

Structures of $[Cu^{II}(1,2\text{-dmIm})_4](ClO_4)_2$ and $[Cu^{II}(Im)_4](SO_4)$ complexes, Gaussian-resolved CD/MCD spectra of PHMcc + N_3^-, abs/MCD spectra of $[Cu^{II}(Im)_4](SO_4)$, additional geometry-optimized structures, ground-state wave functions of Cu_M **1b** and Cu_H **4b**, complete EPR simulation parameters, ligand field fit parameters to $[Cu^{II}(Im)_6]^{2+}$, $[Cu^{II}(H_2O)_6]^{2+}$, and $[Cu^{II}(OH)\{HB(3\text{-}t\text{Bu-}5\text{-}i\text{Prpz})_3\}]$ models, and coordinates of DFT-optimized structures. This material is available free of charge via the Internet at http://pubs.asc.org.

REFERENCES

1. Solomon, E. I., Chen, P., Metz, M., Lee, S.-K., and Palmer, A. E. (2001) Dioxygen Binding, Activation and Reduction to Water, *Angew. Chem., Int. Ed. 40*, 4570−4590.
2. Solomon, E. I., Sundaram, U. M., and Machonkin, T. E. (1996) Multicopper Oxidases and Oxygenases, *Chem. Rev. 96*, 2563−2606.
3. Metz, M., and Solomon, E. I. (2001) Dioxygen Binding to Deoxyhemocyanin: Electron Structure and Mechanism of the Spin Forbidden Two-Electron Reduction of O_2, *J. Am. Chem. Soc. 123*, 4938−4950.

4. Solomon, E. I., Tuczek, F., Root, D. E., and Brown, C. A. (1994) Spectroscopy of Binuclear Dioxygen Complexes, *Chem. Rev. 94*, 827−856.
5. Klinman, J. P. (1996) Mechanism Whereby Mononuclear Copper Protein Functionalizes Organic Substrates, *Chem. Rev. 96*, 2541−2562.
6. Prigge, S. T., Mains, R. E., Eipper, B. A., and Amzel, L. M. (2000) New Insights into Copper Monooxygenase and Peptide Amidation: Structure, Mechanism and Function, *Cell. Mol. Life Sci. 57*, 1236−1259.
7. Kulathila, R., Merkler, K. A., and Merkler, D. J. (1999) Enzymatic Formation of C-Terminal Amides, *Nat. Prod. Rep. 16*, 145−154.
8. Blackburn, N. J. (1993) in *Bioinorganic Chemistry of Copper* (Karlin, K. D., and Tyeklár, Z., Eds.) pp 164−183, Chapman & Hall, New York.
9. Fitzpatrick, P. F., Flory, D. R., and Villafranca, J. J. (1985) 3-Phenylpropenes as Mechanism-Based Inhibitors of Dopamine β-Hydroxylase: Evidence for a Radical Mechanism, *Biochemistry 24*, 2108−2114.
10. Fitzpatrick, P. F., and Villafranca, J. J. (1985) Mechanism-Based Inhibitors of Dopamine β-Hydroxylase Containing Acetylenic or Cyclopropyl Groups, *J. Am. Chem. Soc. 107*, 5022−5023.
11. Miller, S. M., and Klinman, J. P. (1985) Secondary Isotope Effects and Structure−Reactivity Correlations in the Dopamine β-Monooxygenase Reaction: Evidence for a Chemical Mechanism, *Biochemistry 24*, 2114−2127.
12. Wimalasena, K., and May, S. W. (1989) Dopamine β-Monooxygenase Catalyzed Aromatization of 1-(2-Aminoethyl)-1,4-cyclohexadiene: Redirection of Specificity and Evidence for a Hydrogen Atom Transfer Mechanism, *J. Am. Chem. Soc. 111*, 2729−2731.
13. Prigge, S. T., Kolhekar, A. S., Eipper, B. A., Mains, R. E., and Amzel, L. M. (1999) Substrate-mediated Electron Transfer in Peptidylglycine α-hydroxylating Monooxygenase, *Nat. Struct. Biol. 6*, 976−983.
14. Bell, J., Meskini, R. E., D'Amato, D., Mains, R. E., and Eipper, B. A. (2003) Mechanistic Investigation of Peptidylglycine α-Hydroxylating Monooxygenase via Intrinsic Tryptophan Fluorescence and Mutagenesis, *Biochemistry 42*, 7133−7142.
15. Jaron, S., and Blackburn, N. J. (1999) Does Superoxide Channel between the Copper Centers in Peptidylglycine Monooxygenase? A New Mechanism Based on Carbon Monooxide Reactivity, *Biochemistry 38*, 15086−15096.
16. Chen, P., Fujisawa, K., and Solomon, E. I. (2000) Spectroscopic and Theoretical Studies of Mononuclear Copper(II) Alkyl- and Hydroperoxo Complexes: Electronic Structure contributions to Reactivity, *J. Am. Chem. Soc. 122*, 10177−10193.
17. Prigge, S. T., Kolhekar, A. S., Eipper, B. A., Mains, R. E., and Amzel, L. M. (1997) Amidation of Bioactive Peptides: The Structure of Peptidylglycine α-Hydroxylating Monooxygenase, *Science 278*, 1300−1305.
18. Eipper, B. A., Quon, A. S. W., Mains, R. E., Boswell, J. S., and Blackburn, N. J. (1995) The Catalytic Core of Peptidylglycine α-Hydroxylating Monooxygenase: Investigation by Site-Directed Mutagenesis, Cu X-ray Absorption Spectroscopy, and Electron Paramagnetic Resonance, *Biochemistry 34*, 2857−2865.
19. Blackburn, N. J., Concannon, M., Shahiyan, S. K., Mabbs, F. E., and Collison, D. (1988) Active Site of Dopamine β-Hydroxylase. Comparison of Enzyme Derivatives Containing Four and Eight Copper Atoms per Tetramer Using Potentiometry and EPR Spectroscopy, *Biochemistry 27*, 6001−6008.
20. Blackburn, N. J., Rhames, F. C., Ralle, M., and Jaron, S. (2000) Major Changes in Copper Coordination Accompany Reduction of Peptidylglycine Monooxygenase: Implications for Electron Transfer and the Catalytic Mechanism, *J. Biol. Inorg. Chem. 5*, 341−353.
21. Pate, J. E., Ross, P. K., Thamann, T. J., Reed, C. A., Karlin, K. D., Sorrell, T. N., and Solomon, E. I. (1989) Spectroscopic Studies of the Charge Transfer and Vibrational Features of Binuclear Copper(II) Azide Complexes: Comparison to the Coupled Binuclear Copper Active Site in Met Azide Hemocyanin and Tyrosinase, *J. Am. Chem. Soc. 111*, 5198.
22. Tuczek, F., and Solomon, E. I. (1993) Charge-Transfer States of Bridged Transition Metal Dimers: Mono- vs Binuclear Copper Azide Systems with Relevance to Oxy-hemocyanin, *Inorg. Chem. 32*, 2850.
23. Kolhekar, A. S., Keutmann, H. T., Mains, R. E., Quon, A. S. W., and Eipper, B. A. (1997) Peptidylglycine α-Hydroxylating Monooxygenase: Active Site Residues, Disulfide Linkage, and a Two-Domain Model of the Catalytic Core, *Biochemistry 36*, 10901−10909.
24. Bernarducci, E., Bharadwaj, P. K., Krogh-Jespersen, K., Potenza, J. A., and Schugar, H. J. (1983) Electronic Structure of Alkylated Imidazoles and Electronic Spectra of Tetrakis(imidazole)copper(II) Complexes. Molecular Structure of Tetrakis(1,4,5-trimethylimidazole)copper(II) Diperchlorate, *J. Am. Chem. Soc. 105*, 3860−3866.
25. Center for Magnetic Resonance and Department of Mathematics, U. o. Q., Brisbane, Queensland, Australia and Bruker Biospin GmbH, Rheinstetten, Germany. (2003).
26. Solomon, E. I., and Hanson, M. A. (1999) in *Inorganic Electronic Structure and Spectroscopy* (Solomon, E. I., and Lever, A. B. P., Eds.) pp 1−130, John Wiley & Sons, Inc., New York.
27. Frisch, M. J., Trucks, G. W., Schlegel, H. B., Scuseria, G. E., Robb, M. A., Cheeseman, J. R., Zakrzewski, V. G., Montgomery, J. A., Jr., Stratmann, R. E., Burant, J. C., Dapprich, S., Millam, J. M., Daniels, A. D., Kudin, K. N., Strain, M. C., Farkas, O., Tomasi, J., Barone, V., Cossi, M., Cammi, R., Mennucci, B., Pomelli, C., Adamo, C., Clifford, S., Ochterski, J., Petersson, G. A., Ayala, P. Y., Cui, Q., Morokuma, K., Malick, D. K., Rabuck, A. D., Raghavachari, K., Foresman, J. B., Cioslowski, J., Ortiz, J. V., Baboul, A. G., Stefanov, B. B., Liu, G., Liashenko, A., Piskorz, P., Komaromi, I., Gomperts, R., Martin, R. L., Fox, D. J., Keith, T., Al-Laham, M. A., Peng, C. Y., Nanayakkara, A., Gonzalez, C., Challacombe, M., Gill, P. M. W., Johnson, B., Chen, W., Wong, M. W., Andres, J. L., Gonzalez, C., Head-Gordon, M., Replogle, E. S., and Pople, J. A. (1998) *Gaussian 98*, Gaussian, Inc., Pittsburgh, PA.
28. Becke, A. D. (1993) Density-functional thermochemistry. III. The role of exact exchange, *J. Chem. Phys. 98*, 5648.
29. Schaftenaar, G., and Noordik, J. H. (2000) Molden: a pre- and postprocessing program for molecular and electronic structures, *J. Comput.-Aided Mol. Des. 14*, 123.
30. Gorelsky, S. I., and Lever, A. B. P. (2001) *AOmix*, York University, Ontario, Canada.
31. Pavel, E. G. (1997) Magnetic Circular Dichroism Spectroscopic Studies of Mononuclear Non-Heme Iron Sites: Methodology and Applications to Non-Heme Enzymes, Ph.D. Thesis in Chemistry, Stanford University, Stanford, CA.
32. Companion, A. L., and Komarynsky, M. A. (1964) Crystal Field Splitting Diagrams, *J. Chem. Educ. 41*, 257−262.
33. Merkler, D. J., Kulathila, R., Young, S. D., Freeman, J., and Villafranca, J. J. (1993) in *Bioinorganic Chemistry of Copper* (Karlin, K. D., and Tyeklár, Z., Eds.) pp 196−209, Chapman & Hall, New York.
34. Blackburn, N. J., Collison, D., Sutton, J., and Mabbs, F. E. (1984) Kinetic and E.P.R. Studies of Cyanide and Azide Binding to the Copper Sites of Dopamine (3,4-Dihydroxyphenethylamine) β-Monooxygenase, *Biochem. J. 220*, 447−454.
35. Penfield, K. W., Gewirth, A. A., and Solomon, E. I. (1985) Electronic Structure and Bonding of the Blue Copper Site in Plastocyanin, *J. Am. Chem. Soc. 107*, 4519−4529.
36. Gewirth, A. A., Cohen, S. L., Schugar, H. J., and Solomon, E. I. (1987) Spectroscopic and Theoretical Studies of the Unusual EPR Parameters of Distorted Tetrahedral Cupric Sites: Correlations to X-ray Spectral Features of Core Levels, *Inorg. Chem. 26*, 1133−1146.
37. Tolman, W. B., Carrier, S. M., Ruggiero, C. E., Antholine, W. E., and Whittaker, J. W. (1993) in *Bioinorganic Chemistry of Copper* (Karlin, K. D., and Tyeklár, Z., Eds.) pp 406−418, Chapman & Hall, New York.
38. Westmoreland, T. D., Wilcox, D. E., Baldwin, M. J., Mims, W. B., and Solomon, E. I. (1989) Detailed Spectroscopic Analysis of Half-Met Hemocyanins: Mixed-Valent Contributions to Electronic Properties and Structure, *J. Am. Chem. Soc. 111*, 6106−6123.
39. Potenza, M. N., Potenza, J. A., and Schugar, H. J. (1988) Structures of Tetrakis(1,2-dimethylimidazole)M^{II} Doperchlorate (M^{II}=Ni, Cu), *Acta Crystallogr. C44*, 1201−1204.
40. Boswell, J. S., Reedy, B. J., Kulathila, R., Merkler, D. J., and Blackburn, N. J. (1996) Structural Investigation on the Coordination Environment of the Active-Site Copper Centers of Recombinant Bifunctional Peptidylglycine α-Amidating Enzyme, *Biochemistry 35*, 12241−12250.
41. Cotton, F. A. (1990) *Chemical Applications of Group Theory*, 3rd ed., John Wiley & Sons, Inc., New York.

42. Koster, G. F., Dimmock, J. O., Wheeler, B. G., and Statz, H. (1963) *Properties of the Thirty-Two Point Groups*, M.I.T. Press, Cambridge, MA.
43. Piepho, S. B., and Schatz, P. N. (1983) *Group Theory in Spectroscopy with Application to Magnetic Circular Dichroism*, John Wiley & Sons, Inc., New York.
44. Solomon, E. I., Pavel, E. G., Loeb, K. E., and Campochiaro, C. (1995) Magnetic Circular Dichroism Spectroscopy as A Probe of the Geometric and Electronic Structure of Non-Heme Ferrous Enzymes, *Coord. Chem. Rev. 144*, 369−460.
45. Lever, A. B. P. (1984) *Inorganic Electronic Spectroscopy*, 2nd ed., Elsevier Science, Amsterdam, The Netherlands.
46. Penfield, K. W., Gay, R. R., Himmelwright, R. S., Eickman, N. C., Norris, V. A., Freeman, H. C., and Solomon, E. I. (1981) Spectroscopic Studies on Plastocyanin Single Crystals: A Detailed Electronic Structure Determination of the Blue Copper Active Site, *J. Am. Chem. Soc. 103*, 4382−4388.
47. McFadden, D. L., McPhail, A. T., Garner, C. D., and Mabbs, F. E. (1975) Crystal and Molecular Structure, Electron Spin Resonance, and Electronic Spectrum of Hexakis(imidazole)copper(II) Nitrate, *J. Chem. Soc., Dalton Trans.* 263−268.
48. Hitchman, M. A., and Waite, T. D. (1976) Electronic Spectrum of the $Cu(H_2O)_6^{2+}$ Ion, *Inorg. Chem. 15*, 2150−2154.
49. Hitchman, M. A., and Waite, T. D. (1976) Molecular g Values of the $Cu(H_2O)_6^{2+}$ Ion, *Inorg. Chem. 15*, 2155−2158.
50. Fujisawa, K., Kobayashi, T., Fujita, K., Kitajima, N., Moro-oka, Y., Miyashita, Y., Yamada, Y., and Okamoto, K. (2000) Mononuclear Copper(II) Hydroxo Complex: Structural Effect of a 3-Position of Tris(pyrazolyl)borates, *Bull. Chem. Soc. Jpn. 73*, 1797−1804.
51. Ballhausen, C. J. (1962) *Introduction to Ligand Field Theory*, McGraw-Hill Book Company, Inc., New York.
52. Ruggiero, C. E., Carrier, S. M., and Tolman, W. B. (1994) Reductive Disproportionation of NO Mediated by Copper Complexes: Modeling N_2O Generation by Copper Proteins and Heterogeneous Catalysis, *Angew. Chem., Int. Ed. 33*, 895−897.
53. Walsh, A., Walsh, B., Murphy, B., and Hathaway, B. J. (1981) The Structure of Bis(2,2′-bipyridyl)mononitritocopper(II) Tetrafluoroborate Bis(2,2′-bipyridyl)mononitritozinc(II) Nitrate, *Acta Crystallogr. B37*, 1512−1520.
54. Tolman, W. B. (1991) A Model for the Substrate Adduct of Copper Nitrite Reductase and Its Conversion to a Novel Tetrahedral Copper(II) Triflate Complex, *Inorg. Chem. 30*, 4877−4880.
55. Allmann, R., Kremer, S., and Kucharzcyk, D. (1984) The Crystal Structure and EPR g-Tensor of $[Cuterpy(ONO)OH_2]NO_2$ H_2O, *Inorg. Chem. Acta 85*, L19−L21.
56. Jiang, F., Conry, R. R., Bubacco, L., Tyeklár, Z., Jacobson, R. R., Karlin, K. D., and Peisach, J. (1993) Crystal Structure and Electron Spin−Echo Envelope Modulation Study of [Cu(II)(TEPA)-(NO_2)]PF_6 (TEPA=Tris[2-(2-pyridyl)ethyl]amine): A Model for the Purported Structure of the Nitrite Derivative of Hemocyanin, *J. Am. Chem. Soc. 115*, 2093−2102.
57. Szilagyi, R. K., Metz, M., and Solomon, E. I. (2002) Spectroscopic Calibration of Modern Density Functional Methods Using $[CuCl_4]^{2-}$, *J. Phys. Chem. A 106*, 2994−3007.
58. Root, D. E., Mahroof-Tahir, M., Karlin, K. D., and Solomon, E. I. (1998) Effect of Protonation on Peroxo-Copper Bonding: Spectroscopic and Electronic Structure Study of $[Cu_2(UN-O-)-(OOH)]^{2+}$, *Inorg. Chem. 37*, 4838.
59. McGarvey, B. R. (1966) in *Transition Metal Chemistry* (Carlin, R. L., Ed.) pp 89−201, M. Dekker, New York.
60. Stewart, L. C., and Klinman, J. P. (1988) Dopamine Beta-Hydroxylase of Adrenal Chromaffin Granules: Structures and Function, *Annu. Rev. Biochem. 57*, 551−592.
61. Davis, M. I., Wasinger, E. C., Decker, A., Pau, M. Y. M., Vaillancourt, F. H., Bolin, J. T., Eltis, L. D., Hedman, B., Hodgson, K. O., and Solomon, E. I. (2003) Spectroscopic and Electronic Structure Studies of 2,3-Dihydroxybiphenyl 1,2-Dioxygenase: O_2 Reactivity of the Non-Heme Ferrous Site in Extradiol Dioxygenases, *J. Am. Chem. Soc. 125*, 11214−11227.
62. Chen, P., and Solomon, E. I. (2004) Oxygen Activation by the Non-Coupled Binuclear Copper Site in Peptidylglycine α-Hydroxylating Monooxygenase. Reaction Mechanism and Role of the Non-Coupled Nature of the Active Site, *J. Am. Chem. Soc.* published online March 20, 2004, http//dx.doi.org/10.1021/ja031564g.
63. Randall, D. W., George, S. D., Hedman, B., Hodgson, K. O., Fujisawa, K., and Solomon, E. I. (2000) Spectroscopic and Electronic Structural Studies of Blue Copper Model Complexes. 1. Perturbation of the Thiolate-Cu Bond, *J. Am. Chem. Soc. 122*, 11620−11631.
64. Evans, J. P., Ahn, K., and Klinman, J. P. (2003) Evidence That Dioxygen and Substrate Activation Are Tightly Coupled in Dopamine β-Monooxygenase, *J. Biol. Chem. 278*, 49691−49698.

BI0362830